F. Ferrari, A. Tasora, P. Masarati, M. Lavagna
*N-Body Gravitational and Contact Dynamics for Asteroid Aggregation*
Multibody System Dynamics, Vol. 39, N. 1, 2017, p. 3-20
doi:10.1007/s11044-016-9547-2

**Multibody System Dynamics manuscript No.**
(will be inserted by the editor)

# *N*-Body Gravitational and Contact Dynamics for Asteroid Aggregation

**Fabio Ferrari · Alessandro Tasora · Pierangelo Masarati · Michèle Lavagna**

Received: date / Accepted: date

**Abstract** The development of dedicated numerical codes has recently pushed forward the study of $N$-body gravitational dynamics leading to a better and wider understanding of processes involving the formation of natural bodies in the Solar System. A major branch includes the study of asteroid formation: evidence from recent studies and observations support the idea that small and medium size asteroids between 100 m and 100 km may be gravitational aggregates with no cohesive force other than gravity. This evidence implies that asteroid formation depends on gravitational interactions between different boulders and that asteroid aggregation processes can be naturally modeled with $N$-body numerical codes implementing gravitational interactions. This work presents a new implementation of an $N$-body numerical solver. The code is based on Chrono::Engine [1]. It handles the contact and collision of large numbers of complex-shaped objects, while simultaneously evaluating the effect of $N$ to $N$ gravitational interactions. A special case of study is considered, investigating the relative dynamics between the $N$ bodies and highlighting favorable conditions for the formation of a stable gravitationally bound aggregate from a cloud of $N$ boulders. The code is successfully validated for the case of study by comparing relevant results obtained for typical known dynamical scenarios. The outcome of the numerical simulations shows good agreement with theory and observation and suggests the ability of the developed code to predict natural aggregation phenomena.

Politecnico di Milano, Dipartimento di Scienze e Tecnologie Aerospaziali
Via La Masa 34, 20156 Milano, Italy
Tel.: +39 02 23998365
Fax: +39 02 23998334
E-mail: [fabio1.ferrari, pierangelo.masarati, michelle.lavagna]@polimi.it

Università degli Studi di Parma, Dipartimento di Ingegneria Industriale
Viale delle Scienze 181/A, 43100 Parma, Italy
E-mail: alessandro.tasora@unipr.it

**Keywords** $N$-Body Problem · Asteroid Aggregation · Contact Dynamics · Rigid Body · Non-Spherical Shape

## 1 Introduction

Nowadays, small celestial bodies such as asteroids and comets represent the new frontier of the exploration of the Solar System. Space missions aimed at the exploration of these bodies are motivated by great scientific interests, and represent a great challenge for modern space engineering. Recently, the European Rosetta mission [2] highlighted the challenge of landing a probe on the surface of an extremely irregular body such as comet 67P/Churyumov-Gerasimenko [3] (Figure 1(a)), whose shape and mass distribution were completely unknown during the design phase of the mission. The effective design of trajectories to fly a spacecraft in the proximity of an asteroid requires the knowledge of the physical, inertial and dynamical properties of such complex and irregular bodies.

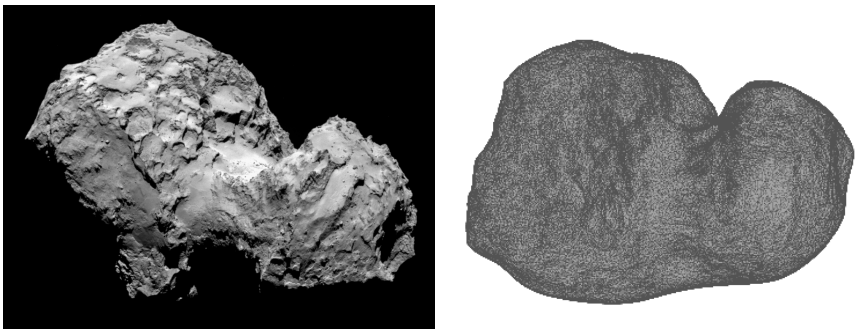

(a) (b)

**Fig. 1** Comet 67P/Churyumov-Gerasimenko (a) picture from Rosetta spacecraft (credits: ESA, 2014) (b) polyhedral shape model.

Few strategies can be adopted to model the gravity field about asteroids according to different levels of accuracy. Classic methods consider a spherical mass distribution of the asteroid and include harmonic expansion of gravitational potential [4] to model the irregularities of the field. Other methods model the asteroid as objects with specific shapes, such as a homogeneous ellipsoid [5] or polyhedron [6, 7]. Figure 1(b) shows an example of a polyhedral model of comet 67P/Churyumov-Gerasimenko. The accuracy of each method depends on the modeled target body and on the application. Typically, each model fits a specific class of asteroids and application range. In the late 1970s, Chapman [8] used the term "rubble pile" to indicate a gravitational aggregate of boulders. Recent studies and observations support the idea that comet nuclei and asteroids between 100 m and 100 km in size may be gravitational

aggregates [9]. Such aggregates have very low tensile strength, possessing no cohesive force other than gravity. Asteroids of this class (gravitational aggregates in the followings) can have up to 40% porosity (void fraction). For this reason, homogeneous mass models of asteroids are usually not suitable to model gravitational aggregates with high accuracy since internal voids can significantly affect the outer field.

This evidence motivates the present work. The ultimate output of this study is to obtain a high accuracy model of the asteroid mass distribution by studying it as a gravitational aggregate. In detail, the purpose is to study the gravitational aggregation process of a cluster of boulders and to investigate favorable conditions for the formation of a stable aggregate. The problem to be investigated is twofold: (a) the study of gravitational aggregation dynamics, and (b) the study of the physical and dynamical properties of the final aggregate. The first aspect includes the analysis and numerical simulation of typical scenarios, for small and medium-size (hundreds of meters) asteroid aggregation, to identify dynamical conditions that lead to the formation of the aggregate or to the dispersion of the particle cloud.

The physical problem is modeled as a classical $N$-body problem, with mutual gravitational interaction between all bodies. Collision detection is implemented and contact forces are included to describe the dynamics of the colliding bodies. The $N$-body problem is a well known mathematical problem, with an established mathematical formulation, but the full comprehension of its solutions and dynamical behavior is still very far from being reached. It has been proved that no analytical solution exists: the problem is characterized by a highly non-linear (chaotic) behavior, which is reflected in a strong dependency of the solution on initial conditions. From the numerical point of view, the $N$-body problem is usually approached using two main classes of codes: $N$-body integrators and $N$-body simulators [10]. Integrators solve the Newtonian equations of motion by computing all $N$ to $N$ gravitational interactions between bodies. Simulators incorporate models of dynamical or physical effects to partially estimate the behavior of the $N$ bodies. As a consequence, the high accuracy of numerical integrators is associated with long computational time, whereas simulators are usually faster. The selection of the algorithm is strictly dependent on the application, namely on the physical phenomenon that must be reproduced. Concerning the accretion of planetesimal and asteroid aggregation processes, relevant implementations include tree codes [11–13], hybrid codes [14], adaptive algorithms of optimal orders [15], systolic algorithms [16] and, more in general, symplectic codes [17–19]. At the time being, typical capabilities of $N$-body integration software include the handling of a few hundred bodies with simple (spherical) shape. Collisions and contact interaction between bodies are often resolved by interfacing with hydrodynamics codes or by implementing hard/soft sphere collision models [9, 20]. The problem is here implemented using the open source Chrono::Engine simulation library (C::E in the following) [1, 21], which is able to handle the contact and collision of large numbers of complex-shaped objects.

After this introductory chapter, the dynamic model and its implementation are shown in Section 2. The set up of numerical simulations is presented in Section 3 and the results are discussed in Section 4. Concluding remarks and future work are summarized in Section 5.

## 2 Dynamics and Implementation

This chapter presents the dynamical model used for the gravitational and contact forces between bodies and the numerical implementation of the code using C::E. From a computational standpoint, the problem is characterized by the need to consider long-time simulations of a large number of interacting bodies, simultaneously subjected to gravity and contact forces. Gravity implies many-to-many interaction, which depends on the inverse of the distance squared. Contact forces require collision detection and the handling of non-smooth problems. C::E has been selected for its peculiar ability to efficiently and effectively simulate the collision and interaction of large numbers of irregularly-shaped bodies.

### 2.1 Gravitational dynamics

The classic Newton's law is implemented to solve for gravitational interactions between the $N$ bodies, where each body moves under the gravitational attraction of all remaining $N$-1 bodies

$$m_i \ddot{\mathbf{R}}_i = G \sum_{j=1, j\neq i}^{N} \frac{m_i m_j}{\|\mathbf{R}_{ij}\|^3} \mathbf{R}_{ij} \qquad \forall i = 1 : N \tag{1}$$

with $\mathbf{R}_i$ representing the position vector of the center of mass of body $i$ in an inertial frame and $\mathbf{R}_{ij} = \mathbf{R}_j - \mathbf{R}_i$, while $m_i$ represents its mass and $G$ is the universal gravitational constant. As shown in Section 3.1, this work investigates the effect of different initial condition sets on the dynamical evolution of a cluster of bodies. Initial conditions are given to initiate the relative distance and velocity between bodies, but also to initiate their absolute state with respect to a given inertial frame ($XYZ$). In particular, the dynamics of the system are investigated when a predefined orbital angular momentum is given about the origin $O$ of the aforementioned inertial frame. In this case, all bodies rotate about $O$ with a constant angular velocity $\boldsymbol{\Omega}$. System (1) can be equivalently written in a rotating frame ($xyz$) that rotates with angular velocity $\boldsymbol{\Omega}$ with respect to the inertial frame

$$m_i \ddot{\mathbf{r}}_i = G \sum_{j=1, j\neq i}^{N} \frac{m_i m_j}{\|\mathbf{r}_{ij}\|^3} \mathbf{r}_{ij} - m_i \boldsymbol{\Omega} \times (\boldsymbol{\Omega} \times \mathbf{r}_i) - 2 m_i \boldsymbol{\Omega} \times \dot{\mathbf{r}}_i \qquad \forall i = 1 : N \tag{2}$$

where $\mathbf{r}_i$ is the position vector of body $i$ in the rotating frame and $\mathbf{r}_{ij} = \mathbf{r}_j - \mathbf{r}_i$. The effect of the rotation is included by adding Coriolis and centrifugal terms

to the equation of motion of the center of mass of the $i$-th body. The addition of a predefined orbital angular momentum to the system is used here to simulate a realistic asteroidal aggregation process, e.g. re-accumulation dynamics of asteroidal fragments after a collision event. In this case, all fragments initially belong to a unique asteroid that spins with a certain angular velocity about its principal inertia axes. After a collision with an external body occurs, fragments are created and scattered away from the main body, but they keep part of the orbital angular momentum they had before the collision when they were part of a unique body. The results obtained in Section 4 can be applied to the subsequent re-accumulation phase, as well as to other asteroid aggregation scenarios.

The code is classified as a numerical *integrator*, since it implements all $N$ to $N$ gravitational interactions between bodies. More in detail, the code implements equations (2). From the numerical point of view, system (2) is an initial value problem and its solution strongly depends on the choice of the initial condition set, namely the initial relative state of each body and angular velocity of the rotating frame. An important feature of gravitational interaction, to be considered from the numerical point of view, is that it is characterized by slow dynamics: for the case of $N$ bodies, the shortest characteristic time can be estimated as follows [13]

$$T \sim \frac{1}{\sqrt{G\rho}} \tag{3}$$

More in details, a particle orbiting a mass $M$ at distance $r$ is known to have orbital characteristic time proper of Keplerian solutions:

$$T \sim \frac{1}{\sqrt{GM/r^3}} \tag{4}$$

In the case of N-body interactions, the fastest dynamics in the system are found when two bodies happen to be very close to each other. The limiting case can be found by assuming $r$ as minimum distance between the two bodies (characteristic size of the body) and $M$ as mass of the body. In this case, the standard Keplerian form can be written as (3), where $\rho \sim M/r^3$ is the material density of the bodies.

A constraint for the integrator is derived from (3): since the dynamics are slow, there is no need of having extremely small time steps of integration. To catch the correct dynamical behavior of the system, the integrator time step shall satisfy

$$t_{step} < \frac{T}{2} = \frac{1}{2\sqrt{G\rho}} \tag{5}$$

For typical values of asteroid material density ranging from 1000 to 4000 kg/m$^3$ [9], the maximum time step results in the order of $10^3$ s.

## 2.2 The multibody model

With respect to collision and contact dynamics, the $N$ bodies are treated as three-dimensional rigid bodies of arbitrary shape, thus each body has rotational degrees of freedom, a tensor of inertia and a mesh that can be used for collision detection. In fact, although (1) could be sufficient to implement a simulation of $N$ point-like masses with long-range gravitational interaction, here we also need to address the case where bodies come into contact during the late stages of aggregation. The assumptions and models used to handle contact dynamics are shortly described here.

We assume a system with $N$ bodies, each with position $\boldsymbol{R}_i$, rotation quaternion $\boldsymbol{\rho}_i$, velocity $\dot{\boldsymbol{R}}_i$, angular velocity $\boldsymbol{\omega}_i$, mass $m_i$, tensor of inertia $I_i$, collision surface $\Omega_i$. We also collect these states into generalized coordinates

$$\boldsymbol{q} = \{\boldsymbol{R}_1^T, \boldsymbol{\rho}_1^T, \boldsymbol{R}_2^T, \boldsymbol{\rho}_2^T, ..., \boldsymbol{R}_N^T, \boldsymbol{\rho}_N^T\}^T \in \mathbb{R}^{7N}$$

$$\boldsymbol{v} = \{\dot{\boldsymbol{R}}_1^T, \boldsymbol{\omega}_1^T, \dot{\boldsymbol{R}}_2^T, \boldsymbol{\omega}_2^T, ..., \dot{\boldsymbol{R}}_N^T, \boldsymbol{\omega}_N^T\}^T \in \mathbb{R}^{6N}$$

where $\dot{\boldsymbol{q}} = \Gamma(\boldsymbol{q})\boldsymbol{v}$. The $\Gamma$ operator translates angular velocities into quaternion derivatives [22]. Masses and inertia moments can be collected in a single, sparse and block-diagonal matrix $M(t) \in \mathbb{R}^{6N \times 6N}$.

External forces acting on the bodies are of two kinds: gravitational forces and contact forces. The first are straightforward, as for each $i$-th body there is a total gravitational force as:

$$\boldsymbol{F}_{G,i} = G \sum_{j=1, j\neq i}^{N} \frac{m_i m_j}{\|\mathbf{R}_{ij}\|^3} \mathbf{R}_{ij} \qquad \forall i = 1 : N \tag{6}$$

We make the assumption that initial bodies are small with respect to final aggregates and that $\boldsymbol{F}_{G,i}$ is applied to the center of mass of each body as if they had a spherical mass distribution. This does not represent a limiting issue: large bodies with odd mass distribution and non-spherical gravitational fields can be created, if needed, at the beginning of the simulation as aggregates of simple bodies.

Contact forces introduce a complication in the time integration of the system. Bodies can collide and re-bounce in collision types ranging from fully elastic to complete inelastic, depending on the selected restitution coefficient (in the present case, inelastic collision has been considered). In fact, because we assume the rigid nature of bodies, contact forces are discontinuous and lead to a non-smooth multibody dynamics problem. Mechanical problems with non-smooth contact forces have been researched by many authors [23–29]. Most formulations fall within the field of Differential Variational Inequalities (DVI) [30], a problem whose time discretization leads to time integrators that must solve a complementarity problem per each time step[1].

[1] As opposed to classical Ordinary Differential Equation (ODE) or Differential Algebraic Equations (DAE) formulations for smooth multibody problems, that just imply one or more linear problems per time step.

Interactions between rigid bodies imply the presence of some constraints: two rigid bodies shall not penetrate each other and, if they are in contact, friction shall act at the interface. A set $\mathcal{K}$ of contacts is computed at each time step. For each contact $k \in \mathcal{K}$ between a pair of bodies $i, j \in N$, we assume that a distance function $\Phi_k(\boldsymbol{q}) = \Phi_{i,j}(\boldsymbol{R}_i, \boldsymbol{\rho}_i, \boldsymbol{R}_j, \boldsymbol{\rho}_j, \Omega_i, \Omega_j)$ can be computed. For rigid bodies, the Signorini unilateral contact constraint holds:

$$\Phi_k(\boldsymbol{q}) \geqslant 0, \quad \hat{\gamma}_k \geqslant 0, \quad \Phi_k(\boldsymbol{q})\hat{\gamma}_{n,k} = 0, \quad \forall k \in \mathcal{K}. \tag{7}$$

where we introduce the force multiplier $\hat{\gamma}_{n,k}$ along the normal direction $\boldsymbol{n}_k$ to the $k$-th contact.

Frictional constraints are described by conic constraints. The Coulomb friction model is used. We introduce the vector of reaction forces in normal and $\mathbf{t}_{u,k}, \mathbf{t}_{v,k}$ tangential directions: $\hat{\boldsymbol{\gamma}}_k = \{\hat{\gamma}_{n,k}, \hat{\gamma}_{u,k}, \hat{\gamma}_{v,k}\}^T$. When a contact is active ($\hat{\gamma}_{n,k} > 0$), normal and tangential forces act at the contact point. The contact force is: $\mathbf{F}_{C,k} = \hat{\gamma}_{n,k}\mathbf{n}_k + \hat{\gamma}_{u,k}\mathbf{t}_{u,k} + \hat{\gamma}_{v,k}\mathbf{t}_{v,k}$ and it is subject to the constraint $\hat{\boldsymbol{\gamma}}_k \in \mathcal{F}_k$, where $\mathcal{F}_k$ is a second-order Lorentz cone of slope $\arctan(\mu_k)$, with $\mu_k$ representing the Coulomb friction coefficient of the $k$-th contact:

$$\mathcal{F}_k = \left\{ \hat{\boldsymbol{\gamma}}_k \mid \mu_k \hat{\gamma}_{n,k} \geqslant \sqrt{\hat{\gamma}_{u,k}^2 + \hat{\gamma}_{v,k}^2} \right\} \quad \subset \mathbb{R}^3$$

As the friction force must be opposed to the sliding direction, if any, we add the following constraint to the Signorini condition:

$$(\hat{\gamma}_{u,k}, \hat{\gamma}_{v,k}) = \operatorname{argmin}_{\sqrt{\hat{\gamma}_{u,k}^2 + \hat{\gamma}_{v,k}^2} \leqslant \mu \hat{\gamma}_{n,k}} (\hat{\gamma}_{u,k}\mathbf{t}_{u,k} + \hat{\gamma}_{v,k}\mathbf{t}_{v,k})^T \mathbf{v}_{T,k} \tag{8}$$

where $\mathbf{v}_{T,k}$ represents the relative tangential velocity at contact $k$. Condition (8) guarantees that the reaction force is dissipative, since the tangential force is opposite to the relative tangential velocity at contact.

Now we introduce the vector of local contact speeds in normal and tangential directions: $\boldsymbol{u}_k = \{u_{n,k}, u_{u,k}, u_{v,k}\}^T$.

Following [31], we introduce $\bar{\boldsymbol{u}}_k = \boldsymbol{u}_k + \{\mu_k |\mathbf{v}_{T,k}|, 0, 0\}^T$ and the dual cones of $\mathcal{F}_k$:

$$\mathcal{F}_k^* = \{\boldsymbol{y} \in \mathbb{R}^n : \langle \boldsymbol{y}, \boldsymbol{x} \rangle \geqslant 0 \quad \forall \boldsymbol{x} \in \mathcal{F}_k\}$$

so we can rewrite (7) and (8), at speed level for active $\Phi_k(\boldsymbol{q}) = 0$ contacts, as a cone complementarity:

$$\hat{\boldsymbol{\gamma}}_k \in \mathcal{F}_k \perp \bar{\boldsymbol{u}}_k \in \mathcal{F}_k^* \tag{9}$$

Finally, we introduce the transposed contact Jacobians $\boldsymbol{D}_{n,k}$, $\boldsymbol{D}_{u,k}$, $\boldsymbol{D}_{v,k} \in \mathbb{R}^{6N}$, we group them in the $D_k = [\boldsymbol{D}_{n,k} | \boldsymbol{D}_{u,k} | \boldsymbol{D}_{v,k}]$ matrix and we write the complete model as the following DVI in generalized coordinates:

$$\begin{aligned} M(t)\frac{d\boldsymbol{v}}{dt} &= \sum_{k \in \mathcal{K}} D_k \hat{\boldsymbol{\gamma}}_k + \boldsymbol{F}_T(t, \boldsymbol{q}, \boldsymbol{v}) \\ \hat{\boldsymbol{\gamma}}_k &\in \mathcal{F}_k \perp \bar{\boldsymbol{u}}_k \in \mathcal{F}_k^*, \quad \forall k \in \mathcal{K}, \Phi_k(\boldsymbol{q}) = 0 \\ \dot{\boldsymbol{q}} &= \Gamma(\boldsymbol{q})\boldsymbol{v} \end{aligned} \tag{10}$$

where $\boldsymbol{F}_T$ is the sum of gyroscopic forces and of the $\boldsymbol{F}_G$ gravitational forces expressed in (6).

In usual approaches to the integration of multibody systems, accelerations are the unknowns to be solved at each time step; instead, here we use a time stepping scheme where the time-discretization of (10) uses variations of velocities as unknowns: this aims at solving the problem as a Measure Differential Inclusion (MDI). The MDI approach [23,32] allows discontinuous events as those that happen because of impacts and sticking friction between rigid bodies, as such it assumes velocities to be functions of bounded variations that could have discontinuities across impulsive events. The time stepping method that we adopt, based on the original scheme in [24], requires the introduction of unknown impulses $\gamma = h\widehat{\gamma}$ for a given timestep $h$, and a stabilization term $\Phi/h$ for $\bar{\boldsymbol{u}}_k^\bullet = \bar{\boldsymbol{u}}_k + \{\frac{\Phi}{h}, 0, 0\}^T$:

$$\boldsymbol{\gamma}_k \in \mathcal{F}_k \perp \bar{\boldsymbol{u}}_k^\bullet(\boldsymbol{v}^{(l+1)}) \in \mathcal{F}_k^* \quad k \in \mathcal{K} \tag{11}$$

$$M(t)\left(\boldsymbol{v}^{(l+1)} - \boldsymbol{v}^{(l)}\right) = \sum_{k\in\mathcal{K}} D_k\widehat{\boldsymbol{\gamma}}_k + h\boldsymbol{F}_T(t, \boldsymbol{q}^{(l)}, \boldsymbol{v}^{(l)}) \tag{12}$$

$$\boldsymbol{q}^{(l+1)} = \Theta(\boldsymbol{q}^{(l)}, \boldsymbol{v}^{(l+1)}) \tag{13}$$

Such time integration scheme consists of three steps (11), (12) and (13), that can be solved in sequence.

In detail, the problem in (11) is a Variational Inequality (VI) and it represents the biggest computational overhead of the entire formulation. After some algebraic manipulations and with some auxiliary assumptions, as shown in [22], it can be formulated as a convex Cone Complementarity Problem (CCP) where $\bar{\boldsymbol{u}}^\bullet = \{\bar{\boldsymbol{u}}_1^\bullet, \ldots, \bar{\boldsymbol{u}}_{n_\mathcal{K}}^\bullet\}^T$ is an affine function $\bar{\boldsymbol{u}}^\bullet = N\boldsymbol{\gamma} + \boldsymbol{r}$ of contact multipliers $\boldsymbol{\gamma} = \{\boldsymbol{\gamma}_1, \ldots, \boldsymbol{\gamma}_{n_\mathcal{K}}\}$:

$$\boldsymbol{\gamma} \in \left(\bigtimes_{k\in\mathcal{K}} \mathcal{F}_k\right) \perp N\boldsymbol{\gamma} + \boldsymbol{r} \in \left(\bigtimes_{k\in\mathcal{K}} \mathcal{F}_k^*\right).$$

The solution of such CCP is a challenging numerical problem. Among the possible methods, we successfully used the spectral projected gradient method [33] and the Nesterov accelerated projected gradient method that we presented in [34].

The problem in (12) can be solved quickly after one computed $\boldsymbol{\gamma}$ from (11), obtaining unknowns $\boldsymbol{v}^{(l+1)}$.

Finally, (13) represents the update of positions and rotations, once $\boldsymbol{v}^{(l+1)}$ is computed. For translations, this boils down to $\boldsymbol{R}_i^{(l+1)} = \boldsymbol{R}_i^{(l)} + h\dot{\boldsymbol{R}}_i^{(l+1)}$. One can see that, for free orbiting bodies not affected by contacts, this together with (12) is equivalent to a symplectic semi-implicit Euler integrator. On the other hand for rotations, which are parametrized via unit quaternions, we prefer to avoid a similar update $\boldsymbol{\rho}_i^{(l+1)} = \boldsymbol{\rho}_i^{(l)} + h\dot{\boldsymbol{\rho}}_i^{(l+1)}$ because such formula might lead to a gradual drift from the unit-length constraint on $\boldsymbol{\rho}_i$. We rather use the exponential map of quaternions to perform $\boldsymbol{\rho}_i^{(l+1)} = \boldsymbol{\rho}_i^{(l)} \exp\left(\{0, \frac{1}{2}\boldsymbol{\omega}_i^{(l+1)} h\}\right)$.

We recall that we consider $\boldsymbol{\omega}_i$ expressed in body local coordinates and that the exponential of an imaginary quaternion is $\exp(\{0, \boldsymbol{b}\}) = \left\{\cos|\boldsymbol{b}|, \frac{\boldsymbol{b}}{|\boldsymbol{b}|}\sin|\boldsymbol{b}|\right\}$, so our incremental update of rotations is implemented as a product between two unit quaternions:

$$\boldsymbol{\rho}_i^{(l+1)} = \boldsymbol{\rho}_i^{(l)} \left\{\cos\frac{1}{2}|\boldsymbol{\omega}_i^{(l+1)}|h, \frac{\boldsymbol{\omega}_i^{(l+1)}}{|\boldsymbol{\omega}_i^{(l+1)}|}\sin\frac{1}{2}|\boldsymbol{\omega}_i^{(l)}|h\right\}$$

This is a special case of Lie group integrator and it preserves the unit-length property of $\boldsymbol{\rho}_i$; more details on integration of rotations can be found in [35, 36].

The interested reader can refer to [37–39] for further details and discussion on how to solve the DVI of (10).

### 2.3 Implementation

The dynamics of the $N$ bodies is implemented using the C::E library. We leveraged the fact that such library is an open-source project, and we customized some features according to our needs. In particular we implemented some functions that target the specific case where rigid bodies are described by convex hulls.

In our implementation, the shape $\Omega_i$ of the $i$-th body is described by a convex hull, which is defined by a finite set of vertexes $\mathcal{H}_i$, each expressed in the local coordinate system of the body[2]. These vertexes define a unique polytope in $\mathbb{R}^3$.

We compute the faceted representation of such polytopes as a triangle mesh in a preprocessing stage using a fast convex hull algorithm [40]. Such triangle mesh is needed for two reasons. First, it is used to compute the center of mass, the tensor of inertia $I_i$ and the mass $m_i$ of the body given its shape and density, using a Gauss quadrature. Second, it is used for the visualization of the body during the simulation.

We remark, however, that we do not use these triangle meshes for computing collisions between a pair of $i, k$ objects. Instead, we run the GJK algorithm directly on the $\mathcal{H}_i$ and $\mathcal{H}_j$ set of vectors, as the only needed information required during the GJK iteration is the computation of the so called *supporting vertex* along a given direction for a limited number of refinements [41]. If the number of vertexes in each $\mathcal{H}$ is moderate, an efficient method to compute the supporting vertex is simply to iterate through the vertex positions and compute the largest dot product along a direction.

The standard GJK algorithm is not robust in the case where the polytopes are inter-penetrating. We avoid this issue by performing the collision detection between convex hulls that have been shrunk by a given small threshold $\eta$, then the computed contact points are offset by $\eta$ along the normals for the contact

[2] Concave shapes can be defined as well, by using convex decompositions. However we assume that our initial bodies have only convex shapes.

dynamics computations. This done, the shrunk polytopes are always separated by a distance $\approx 2\eta$, generally bigger than the inter-penetration that might happen if the solver is not able to satisfy $\Phi_k(\boldsymbol{q}) \geqslant 0$ exactly. Note that this is equivalent to performing a collision detection between the two Minkowski sums $\mathcal{H}_i + \mathcal{S}(\eta)$ and $\mathcal{H}_j + \mathcal{S}(\eta)$, where $\mathcal{S}(\eta)$ is a ball in $\mathbb{R}^3$ with radius $\eta$.

Another issue of the GJK algorithm is that it computes a single contact point, however multiple contact points might be needed in singular cases such as when co-planar faces come into contact. This problem is solved by perturbing the two convex hulls with small random rotations and by adding the found contacts into a manifold that persists between time steps.

Since it is not practical to search for contact points for all possible $i, k$ pairs of bodies when $N$ is large, collision detection is implemented into two steps. A preliminary stage, called *broad-phase collision detection*, identifies $i, k$ pairs whose bounding boxes are near enough; far pairs are discarded. In the second step, called *narrow-phase*, precise contacts are detected using the GJK algorithm on the pre-selected pairs of bodies.

We can define various types of statistical distributions for the geometric properties of the shapes. In our tests, during the initialization stage of the simulation, each body is created as a convex hull with a randomized amount of vertexes distributed randomly according to a given average and minimum particle size. The bodies are randomly positioned within a cubic grid, whose side length is representative of the initial dispersion of the boulders. As mentioned, the full rigid body motion is integrated and computed to correctly reproduce contact dynamics.

Finally, during the simulation loop, a simple algorithm computes each $N$ to $N$ gravitational force to be added to the the $\boldsymbol{F}_T$ term of (10), to reproduce the motion of the center of mass of each body.

## 3 NUMERICAL SIMULATIONS

This Section presents the simulations performed to characterize the process of asteroidal aggregation from a cloud of boulders, highlighting the degrees of freedom of the problem and the assumptions made while selecting the case of study.

### 3.1 Simulation parameters

Several parameters have to be set to initiate the simulation of the asteroid aggregation process. In particular, to simulate realistic scenarios it is important to carefully select the physical properties of the $N$ bodies and to consistently initiate their dynamics.

Initial conditions play an extremely important role when dealing with $N$-body dynamics. The set of initial conditions includes the initial state of all $N$ bodies. As described in Section 2.1, the state of all bodies is expressed in

a rotating frame that rotates with a given angular velocity $\boldsymbol{\Omega}$ with respect to an inertial reference. In addition, the relative state of each body, namely their position and orientation, as well as their linear and angular velocity, are initialized with respect to the rotating reference frame. Initial conditions are given at *time zero*, or $t_0$ in the following.

From the numerical point of view, the choice of the number of bodies is crucial, since it has great impact on the computational effort. For an integrator, the cost of evaluating gravity is $N^2$. For this reason, typical capabilities of numerical integrators are often limited to few hundreds of bodies. The computational cost can be reduced by clustering the gravitational effect of bodies through domain decomposition. In this case, the cost can be reduced to $N \log N$ (N-body simulators [13]).

### 3.2 Case of study

The case of study is presented in this Section. The parameters have been selected to simulate the aggregation process of common asteroids of small/medium size, with a characteristic size of hundreds of meters. The physical properties of the asteroids are chosen among typical values of objects belonging either to the main asteroid belt or to the Near Earth Asteroids (NEA) population [42, 43].

Table 1 summarizes all simulation parameters used to obtain the results presented in Section 4. In the simulations, 200 bodies are randomly generated in a three-dimensional cube whose side is 5 km long. Bodies are medium size boulders of 130 m characteristic size on average; the size of the smallest ones is 40 m. As mentioned earlier, this is likely the case of re-accumulation after fragmentation due to a collision event. The aggregate is then a "rubble pile" of loosely aggregated boulders. The material density has been set to 3000 kg/m$^3$, which is typical for metallic-based asteroids [9]. As discussed in Section 2.1, gravity interactions are slow; the integrator time step can be of the order of $10^3$ s. However, a time step of 10 s is chosen, to correctly integrate collision dynamics. In fact, they are much faster and need shorter integration time steps. With these figures, aggregation processes reach a stable configuration after a transient of few tens of hours, which correspond to computational times in the order of a few minutes.

**Table 1** Simulation parameters.

| **Parameter** | **Symbol** | **Value** |
|---|---|---|
| number of bodies | $N$ | 200 |
| characteristic size of bodies [min-average] | $L^*$ | 40-130 $m$ |
| material density | $\rho$ | 3000 $kg/m^3$ |
| initial position cube side length | $L_0$ | 5 $km$ |
| integration time step | $t_{\text{step}}$ | 10 $s$ |

Simulations are performed for different sets of initial conditions. In particular, the norms of the linear and angular velocity of each body range from 0 (no relative motion between bodies), to the maximum values specified in Table 2. Similarly, different cases have been explored concerning the norm of the angular velocity of the rotating frame, which ranges from 0 to the maximum value in Table 2. Maximum values specified in Table 2 are identified as thresholds above which there is no aggregation of the bodies, which are scattered apart from each other by too high relative velocities or centrifugal force.

**Table 2** Range of values for initial conditions set.

| **Parameter** | **Symbol** | **Max value** |
|---|---|---|
| linear relative velocity of bodies | $v_0$ | $0.15\ m/s$ |
| angular relative velocity of bodies | $\omega_0$ | $10^{-2}\ rad/s$ |
| angular velocity of rotating frame | $\Omega$ | $5 \cdot 10^{-5}\ rad/s$ |

Table 2 defines boundaries on the magnitude of the velocities. Without any loss of generality, the inertial frame $(XYZ)$ is oriented such that $\boldsymbol{\Omega}$ is directed towards the positive $Z$ axis, with $\boldsymbol{\Omega} = \Omega\hat{\mathbf{Z}} = \Omega\hat{\mathbf{z}}$,

$$\boldsymbol{\Omega} = \Omega \begin{Bmatrix} 0 \\ 0 \\ 1 \end{Bmatrix} \tag{14}$$

Concerning the linear and angular velocity of each body, their direction is randomly generated.

The simulation campaign is performed by imposing to the system several initial condition sets, in order to cover different aggregation scenarios and to explore the combined effects between the initial conditions. Table 3 summarizes all simulation sets considered. IDs are specified for each simulation set, to be referred during the analysis of results (Section 4).

**Table 3** Simulation sets.

| **Simulation set** | **ID** | $v_0\ [m/s]$ | $\omega_0\ [rad/s]$ | $\Omega\ [rad/s]$ |
|---|---|---|---|---|
| 0 - no initial motion | 0 | 0 | 0 | 0 |
| 1 - single parameter | 1.1 | $0 - 0.15$ | 0 | 0 |
| | 1.2 | 0 | $0 - 10^{-2}$ | 0 |
| | 1.3 | 0 | 0 | $0 - 5 \cdot 10^{-5}$ |
| 2 - double parameter | 2.1 | $0 - 0.15$ | $0 - 10^{-2}$ | 0 |
| | 2.2 | $0 - 0.15$ | 0 | $0 - 5 \cdot 10^{-5}$ |
| | 2.3 | 0 | $0 - 10^{-2}$ | $0 - 5 \cdot 10^{-5}$ |
| 3 - all parameters | 3 | $0 - 0.15$ | $0 - 10^{-2}$ | $0 - 5 \cdot 10^{-5}$ |

The case with no initial motion between bodies and no rotation imposed is marked ID '0'. The first simulation set (ID '1') includes the analysis of the

effect of one initial condition at a time, with the remaining set to zero. The second set (ID '2') analyzes the effect of two parameters at a time. Finally, the third set of simulations (ID '3') investigates the case of simultaneously fully perturbed initial condition space.

## 4 Results

The results of the aggregation simulations discussed in Section 3 are shown here. The first part of the Section discusses the dynamical evolution of the system, up to the formation (or non-formation) of a stable aggregate (Section 4.1). The aggregation process is studied by looking at the time profile of the orbital angular momentum of the $N$-body system, and by monitoring the evolution of the relative position of all bodies. The last part of the Section focuses on what happens after the transient. In case the system has converged to a stable asteroidal aggregate, the resulting physical and geometrical properties are studied and compared to the properties of known asteroids. Shape and inertia properties of the aggregate and their dependence on initial conditions are investigated. Results are shown in Section 4.2 for all simulation sets. Significant quantities extracted from the simulation scenarios include the bulk density (mean density, including void fraction) of the aggregate, its inertial elongation (ratio between maximum and minimum principal inertia moments) and rotation state.

### 4.1 Aggregation dynamics

An example of aggregation sequence is shown in Figure 2 for case ID '0'. The $N$ bodies are driven solely by their mutual attraction, with no effects due to rotation of the reference frame. When boulders start to interact, few small bodies are scattered away because of collisions, but a stable aggregate eventually forms, collecting 193 bodies out of 200.

Figures 3 and 4 show the time profile of the orbital angular momentum of the system $\mathbf{H}$ with respect to the origin of the inertial frame, computed as the vectorial sum of orbital angular momenta $\mathbf{h}_i$ of the $N$ bodies

$$\mathbf{H} = \sum_{i=1}^{N} \mathbf{h}_i = \sum_{i=1}^{N} m_i \mathbf{r}_i \times \mathbf{v}_i \tag{15}$$

The orbital angular momentum $\mathbf{h}_i$ refers to the orbital motion of the center of mass of the $i$-th body, where $\mathbf{r}_i$ and $\mathbf{v}_i$ are its velocity and position with respect to the origin of the inertial frame. The contribution due to the spinning motion of the $i$-th body is not accounted in $\mathbf{h}_i$. In the case of stable aggregate formation, the orbital angular momentum of the $N$-body system is also the rotational spinning angular momentum of the final aggregate. For this reason, $\mathbf{H}$ is also referenced as rotational energy of the aggregate.

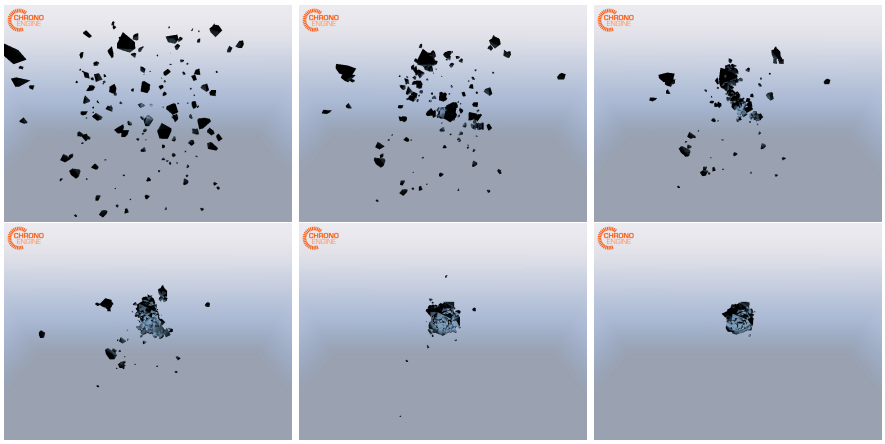

**Fig. 2** Aggregation sequence: case ID '0'.

The norm and the three Cartesian components of $\mathbf{H}$ are shown as a function of simulation time. Case ID '0' is shown in Figure 3(a). At $t_0$, the system is at rest; after a few hours, the first collisions between bodies take place. Most of the collisions occur between 5 and 10 hours after $t_0$. After the transient, the system turns into a single aggregate. The system is initially at rest and after the aggregation process, the final aggregate rotates with a period of about $10^3$ hours (slow rotator). A different case, extracted from set ID 1.3, is shown in Figure 3(b). In this case, the center of mass of the $N$ bodies are initially provided with a common orbital angular velocity ($\Omega = 1.5 \cdot 10^{-5}$ rad/s). The orbital energy of the system is partially dissipated by collision events (between 5 and 10 hours after $t_0$), but in the end most of it is converted to rotational energy of the final aggregate. The final cluster rotates with a period of a few hours (fast rotator).

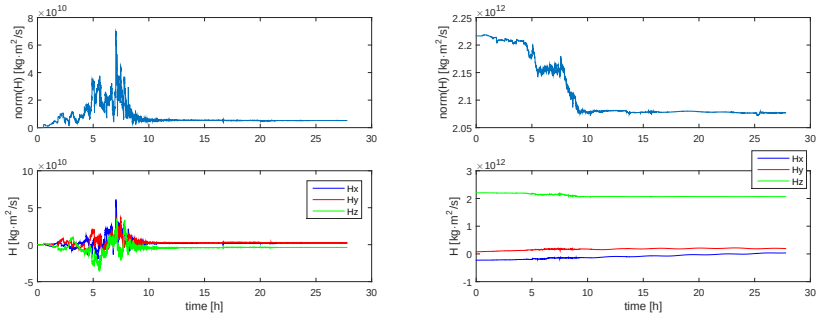


(a) (b)

**Fig. 3** Orbital angular momentum of the $N$-body system: (a) case ID '0' (b) case extracted from set ID '1.3' ($\Omega = 1.5 \cdot 10^{-5}$).

Figure 4(a) shows a simulation case extracted from set ID 1.2. The bodies are provided with a given spinning velocity about their body axes ($\omega_0 = 4{\cdot}10^{-3}$ rad/s). The spinning state of each single body is transmitted between boulders through collisions up to the formation of a single aggregate, which have nonzero angular velocity despite the absence of initial orbital motion of the $N$ bodies. In this specific case, the final aggregate is left with a rotation period of some tens of hours (slow rotator). The effect of combined initial conditions in $\omega_0$ and $\Omega$ is shown in Figure 4(b). The effect due to collisions of dissipating the kinetic energy associated with rotation and of transferring orbital angular momentum among bodies is balanced in this case. The orbital angular momentum of the system stabilizes at about its initial value after the collisions transient. The resulting aggregate is a fast-spinning asteroid.

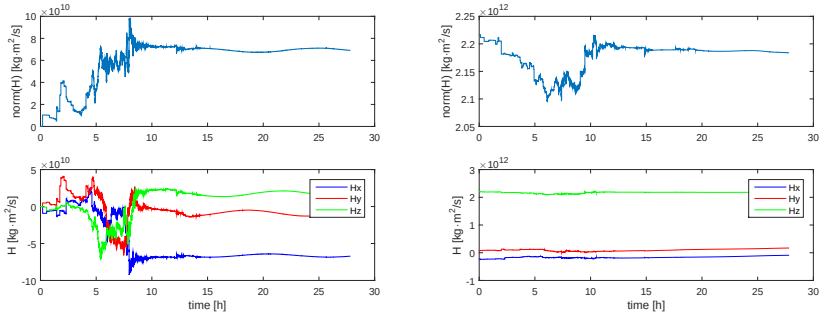


**Fig. 4** Orbital angular momentum of the $N$-body system: (a) $\omega_0 = 4 \cdot 10^{-3}$ rad/s (from set ID '1.2') (b) $\omega_0 = 7 \cdot 10^{-3}$,$\Omega_0 = 1.5 \cdot 10^{-5}$ rad/s (from set ID '2.3').

Maximum breakup values (Table 2) identify the values of $v_0$, $\omega_0$ and $\Omega$ above which no aggregation occurs for the case of study specified in Table 1. The results in terms of breakup values show good agreement with data from the literature: as mentioned in [9], no stable aggregate larger than 200 m is observed to spin faster than critical breakup period, which is approximately 2.2 h for strength-less bodies of density $\sim$3000 kg/m$^3$. Also, aggregation is found for relative speeds between fragments lower than surface escape velocity from the stable aggregate, which is found in the range between 0.4 and 0.8 m/s for the case under study.

The formation of more than one aggregate has been observed when initial conditions are close to their maximum breakup values. In some cases, initial conditions combine to peculiar configurations: Figure 5 shows two examples of the formation of a binary asteroid system (two main aggregates).

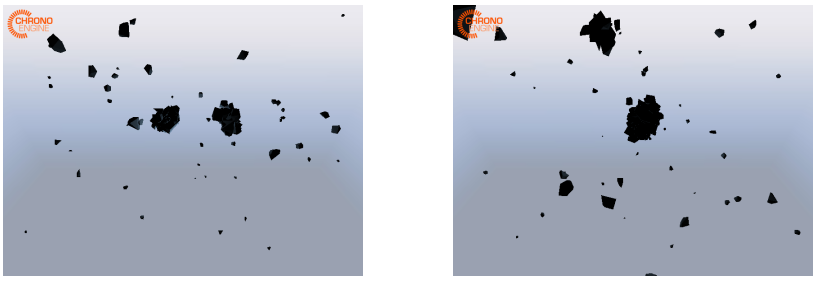

**Fig. 5** Examples of binary asteroid formation, extracted from simulation set ID 2.3 and ID 2.2.

### 4.2 Properties of the final aggregate

Different kinds of aggregates have been obtained from the simulation campaign. This Section identifies the properties of the aggregates and compares them with known asteroids to verify the ability of the numerical code of representing gravitational aggregation phenomena.

After its stabilization, the aggregate is considered as a single asteroid. The shape of the aggregate is found by enveloping it using an alpha shape algorithm [44]. Intuitively, the alpha shape algorithm finds the enveloping surface of the aggregate by rolling a sphere of radius $\alpha$ over the cluster of points. The value of $\alpha$ influences the final result, by constraining the path of the rolling sphere, with $\alpha = \infty$ being equivalent to the convex hull representation. Once the asteroid is identified, its characteristics are studied. Significant properties of asteroids are here briefly defined. The first quantity considered is the *inertial elongation* (or simply *elongation* in the following) $\lambda$, that is defined as the ratio between the maximum and the minimum principal inertia moments. It is always greater than or equal to one: the larger $\lambda$ is, the more elongated the asteroid is. Note that this property refers to the mass distribution of the asteroid, not to its geometry. An important quantity for the case of asteroids is the *bulk density* $\rho_b$, that refers to the mean density of the asteroid, including internal voids. Accordingly, the porosity $P$ is defined as

$$P = 1 - \frac{\rho_b}{\rho} \tag{16}$$

where $\rho$ is the material density (Table 1). In the following, $T_{\text{agg}}$ is used to indicate the period of rotation of the aggregate, $M_{\text{agg}}$ its total mass, and $N_{\text{agg}}$ the number of bodies (out of 200) in the final aggregate.

Figure 6 shows how inertial elongation, rotation period and number of bodies in the aggregate are affected by initial conditions on $v_0$ (blue asterisks), $\omega_0$ (green stars) and $\Omega$ (red diamonds) for the case of study (Table 1). Exponential or polynomial fitting curves are displayed to separately show the trend of each contribution. The values of the initial conditions refer to a normalized range on the abscissa: each parameter ranges from 0 to 1, with 0 as their minimum

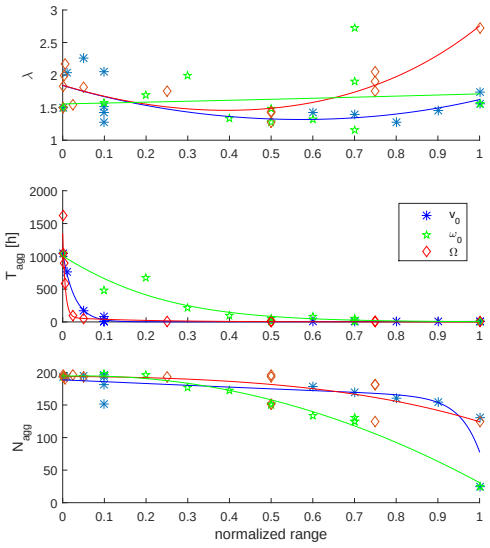


**Fig. 6** Characteristics of the final aggregate as a function of normalized initial conditions: simulation results and best fitting curves.

value ($v_0 = \omega_0 = \Omega = 0$) and 1 their maximum value ($v_0 = v_{0_{\max}}$, $\omega_0 = \omega_{0_{\max}}$, $\Omega = \Omega_{\max}$ from Table 2). The upper plot shows that high elongations are obtained for high $\Omega$ or for low $v_0$, while no precise trend can be derived for $\omega_0$. On the other plots, all parameters are observed to share a common trend characterizing their effect on rotation period and number of bodies in the aggregate. As far as the former is concerned, small relative motion and rotation produce slowly rotating asteroids and vice versa: fast rotators are formed when the bodies are initialized with high angular and linear velocities. In particular, within the validity domain of this case of study, $\Omega$ is observed to produce the strongest effect and $\omega_0$ the weakest one. As for the last case, the number of bodies aggregating in the final asteroid decreases as velocities increase, with $\omega_0$ playing a dominant role.

Figure 7 shows simulation results that correlate the rotation period of the asteroid to its elongation and total mass. Results are shown on semi-logarithmic plots (the rotation period scale is logarithmic). A clear trend can be extracted from the plot on the right: as far as gravitational aggregates are concerned, smaller asteroids rotate faster than more massive ones. This is found in agreement with balancing between centrifugal force and gravitational attraction predicted by the theory [9].

Figures 8 and 9 show examples of asteroids obtained by enveloping all aggregating bodies after the dynamical transient. Minimum (Figure 8(a)) and maximum (Figure 8(b)) elongation cases are shown, in a population of aster-

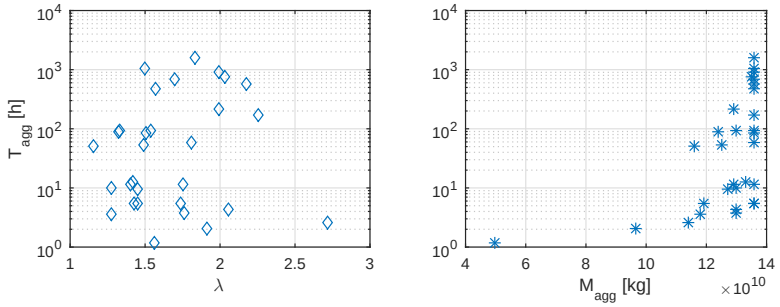


**Fig. 7** Simulation results: rotation period as a function of inertial elongation and total mass in the asteroid population.

oids ranging from quasi-spherical shapes ($\lambda_{\min} \simeq 1.15$) to highly elongated ones ($\lambda_{\max} \simeq 2.7$).

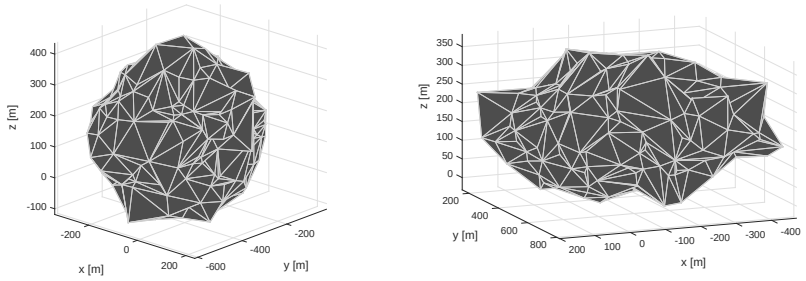


(a) (b)

**Fig. 8** Shape of the final aggregate: (a) minimum (from set ID '1.2') and (b) maximum (from set ID '2.3') inertial elongation case.

For what concerns the porosity (or equivalently the bulk density) of the aggregates, the results show that very little variability exists for the case of study. Porosity is found between 34% and 40% for all large stable aggregates found, corresponding to $\rho_b \simeq 1900$ kg/m$^3$. This is found to be in good agreement with theory and observations concerning asteroids porosity fraction after shattering and reassembling, estimated to be within 20% and 40% [9]. A different result is obtained for the case of the small aggregate depicted in Figure 9(b), for which $P \simeq 14\%$, corresponding to $\rho_b \simeq 2500$ kg/m$^3$. This result agrees with general trend observing that smaller asteroids are more compact, with a lower fraction of interior voids [9]. The lower level of porosity, compare to what reported in [9] can be explained by the low number of bodies forming the final aggregate: only 25 out of 200 bodies are found in the final stable aggregate,

while aggregates with higher porosity have more than 125 bodies in the final aggregate.

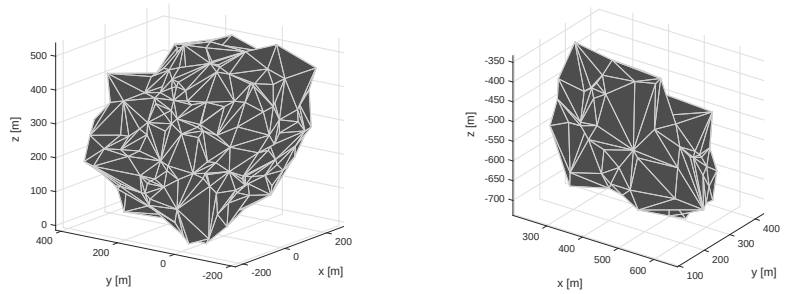


(a) (b)

**Fig. 9** Shape of the final aggregate: (a) minimum (from set ID '1.2') and (b) maximum (from set ID '2.1') bulk density.

## 5 Conclusions

A new implementation is presented to deal with $N$-body gravitational dynamics, including contacts between bodies. The capabilities of C::E are exploited and customized to handle the dynamics of bodies of complex shape.

To test and validate the implementation, significant scenarios have been analyzed in the framework of asteroid formation processes. Different sets of initial conditions have been investigated. The initial dynamical state of the $N$ bodies is found to play a fundamental role in the evolution of the cloud of boulders. In detail, the state of the $N$ bodies has been initialized by either imposing no initial relative motion between them, or by imposing a given rotational and relative motion. The presented results show good agreement with theoretical predictions and observations, and suggest the ability of the numerical code to predict natural aggregation phenomena.

The cost of evaluating gravity is $N^2$. It can be reduced to $N \log(N)$ by clustering the interactional effect between far clusters of bodies. The current phase of the project entails the setup of the procedure. For this reason, no optimization has been performed yet. The partitioning of the domain using octrees, and the GPU-based parallelization of gravitational and contact forces computation will be pursued in a subsequent phase. This promises to grant the capability of handling a higher number of bodies, extending the possibility to simulate different dynamical scenarios such as impact and disruption ones.

Future applications will include the simulation of orbital dynamics about gravitational aggregates. The outcome of the aggregation process will serve as a high-fidelity model of the asteroid's mass distribution. Space mission scenarios

will be implemented to compute and simulate trajectories of spacecraft under the complex gravity field of such highly irregular bodies.

## References


1. A Tasora, D Negrut, R Serban, H Mazhar, T Heyn, A Pazouki, and D Melanz. Chrono::engine web pages at projectchrono.org, 2006.
2. J Biele and S Ulamec. Capabilities of philae, the rosetta lander. *Space Science Review*, 138:275–289, 2008.
3. E Heggy, E M Palmer, W Kofman, S M Clifford, K Righter, and A Hrique. Radar properties of comets: Parametric dielectric modeling of comet 67p/churyumovgerasimenko. *Icarus*, 221:925–939, 2012.
4. W M Kaula. *Theory of Satellite Geodesy.* Blaisdell, Waltham MA, 1966.
5. D J Scheeres. Dynamics about uniformly rotating triaxial ellipsoids: Applications to asteroids. *Icarus*, 110:225–238, 1994.
6. R A Werner and D J Scheeres. Exterior gravitation of a polyhedron derived and compared with harmonic and mascon gravitation representations of asteroid 4769 castalia. *Celestial Mechanics and Dynamical Astronomy*, 65:313–344, 1997.
7. D J Scheeres, S J Ostro, R S Hudson, E M DeJong, and S Suzuki. Dynamics of orbits close to asteroid 4179 toutatis. *Icarus*, 132:53–79, 1998.
8. C R Chapman. Asteroid collisions, craters, regolith and lifetimes. *In Asteroids: An Exploration Assessment. NASA Conf. Publ.*, 2053:145–160, 1978.
9. D C Richardson, Z M Leinhardt, H J Melosh, W F Bottke Jr., and E Asphaug. Gravitational aggregates: Evidence and evolution. *Asteroids III, University of Arizona Press*, pages 501–515, 2002.
10. A Morbidelli. Modern integrations of solar system dynamics. *Annual Reviews of Earth and Planetary Sciences*, 30, 2002.
11. J Stadel. *Cosmological N-body simulations and their analysis.* PhD thesis, University of Washington, Seattle, WA, USA, 2001.
12. D C Richardson, T Quinn, J Stadel, and G Lake. Direct large-scale n-body simulations of planetesimal dynamics. *Icarus*, 143:45–59, 2000.
13. D C Richardson, P Michel, K J Walsh, and K W Flynn. Numerical simulations of asteroids modelled as gravitational aggregates. *Planetary and Space Science*, 57:183–192, 2009.
14. S J Aarseth. Nbody2: A direct n-body integration code. *New Astronomy*, 6:277–291, 2001.
15. C D Pruett, J W Rudmin, and J M Lacy. An adaptive n-body algorithm of optimal order. *Journal of Computational Physics*, 187:298–317, 2003.
16. E N Dorband, M Hemsendorf, and D Merritt. Systolic and hyper-systolic algorithms for the gravitational n-body problem, with an application to brownian motion. *Journal of Computational Physics*, 185:484–511, 2003.
17. J Wisdom and M Holman. Symplectic maps for the n-body problem. *Astronomical Journal*, 102:1528–1538, 1991.
18. M J Duncan, H F Levison, and M H Lee. A multiple time step symplectic algorithm for integrating close encounters. *Astronomical Journal*, 116:2067–2077, 1998.
19. J E Chambers. A hybrid symplectic integrator that permits close encounters between massive bodies. *Monthly Notices of the Royal Astronomical Society*, 304:793–799, 1999.
20. P Michel, P Tanga, W Benz, and D C Richardson. Formation of asteroid families by catastrophic disruption: Simulations with fragmentation and gravitational reaccumulation. *Icarus*, 160:10–23, 2002.
21. H Mazhar, T Heyn, A Pazouki, D Melanz, A Seidl, A Barthlomew, A Tasora, and D Negrut. Chrono: A parallel multi-physics library for rigid-body, flexible-body and fluid dynamics. *Mechanical Sciences*, 2013.
22. M Anitescu and A Tasora. An iterative approach for cone complementarity problems for nonsmooth dynamics. *Computational Optimization and Applications*, 47(2):207–235, 2010.

23. J.J. Moreau. Numerical aspects of the sweeping process. *Computer Methods in Applied Mechanics and Engineering*, 177(3-4):329 – 349, 1999.
24. D. E. Stewart and J.C. Trinkle. An implicit time-stepping scheme for rigid body dynamics with inelastic collisions and coulomb friction. *International J. Numer. Methods Engineering*, 39(15):281–287, 1996.
25. Florian A. Potra, Mihai Anitescu, Bogdan Gavrea, and Jeff Trinkle. A linearly implicit trapezoidal method for integrating stiff multibody dynamics with contact and friction. *International Journal for Numerical Methods in Engineering*, 66(7):1079–1124, 2006.
26. M. Renouf and P. Alart. Conjugate gradient type algorithms for frictional multi-contact problems: applications to granular materials. *Computer Methods in Applied Mechanics and Engineering*, 194(18-20):2019–2041, May 2005.
27. Remco Leine and Christoph Glocker. A set-valued force law for spatial coulomb-contensou friction. *European Journal of Mechanics*, 22(2):193–216, 2003.
28. Vincent Acary and Bernard Brogliato. *Numerical methods for nonsmooth dynamical systems: applications in mechanics and electronics*, volume 35. Lect. N. App. Comput. Mech. 35 Springer Verlag, 2008.
29. Alessandro Tasora and Mihai Anitescu. A complementarity-based rolling friction model for rigid contacts. *Meccanica*, 48(7):1643–1659, 2013.
30. J. S. Pang and D. E. Stewart. Differential variational inequalities. *Mathematical Programming*, 113:1–80, 2008.
31. G. De Saxc and Z.-Q. Feng. Recent advances in contact mechanics the bipotential method: A constructive approach to design the complete contact law with friction and improved numerical algorithms. *Mathematical and Computer Modelling*, 28(4):225 – 245, 1998.
32. Friedrich Pfeiffer and Christian Glocker. *Multibody Dynamics with Unilateral Contacts*. John Wiley, New York City, 1996.
33. Toby Heyn, Mihai Anitescu, Alessandro Tasora, and Dan Negrut. Using krylov subspace and spectral methods for solving complementarity problems in many-body contact dynamics simulation. *International Journal for Numerical Methods in Engineering*, 95(7):541–561, 2013.
34. Hammad Mazhar, Toby Heyn, Dan Negrut, and Alessandro Tasora. Using nesterov's method to accelerate multibody dynamics with friction and contact. *ACM Trans. Graph.*, 34(3):32:1–32:14, May 2015.
35. Hans Munthe-Kaas. High order runge-kutta methods on manifolds. *Applied Numerical Mathematics*, 29(1):115 – 127, 1999. Proceedings of the NSF/CBMS Regional Conference on Numerical Analysis of Hamiltonian Differential Equations.
36. Zdravko Terze, Andreas Müller, and Dario Zlatar. Singularity-free time integration of rotational quaternions using non-redundant ordinary differential equations. *Multibody System Dynamics*, pages 1–25, 2016.
37. A Tasora and M Anitescu. A matrix-free cone complementarity approach for solving large-scale, nonsmooth, rigid body dynamics. *Computer Methods in Applied Mechanics and Engineering*, 200:439–453, 2011.
38. A Tasora, D Negrut, and M Anitescu. Large-scale parallel multi-body dynamics with frictional contact on the graphical processing unit. *Journal of Multi-body Dynamics*, 222:315–326, 2008.
39. A Tasora and M Anitescu. A convex complementarity approach for simulating large granular flows. *Journal of Computational and Nonlinear Dynamics*, 5:1–10, 2010.
40. C Bradford Barber, David P Dobkin, and Hannu Huhdanpaa. The quickhull algorithm for convex hulls. *ACM Transactions on Mathematical Software (TOMS)*, 22(4):469–483, 1996.
41. S.S. Keerthi E.G. Gilbert, D.W. Johnson. A fast procedure for computing the distance between complex objects in three-dimensional space. *Robotics and Automation*, 4(2):193–203, 1988.
42. R. Johnston. Johnston's archive web pages at johnstonsarchive.net, 2016.
43. NASA JPL. Jpl small-body database web pages at ssd.jpl.nasa.gov, 2016.
44. H Edelsbrunner and E P Mücke. Three-dimensional alpha shapes. *Transactions on Graphics*, 13(1):43–72, 1994.